Electron-phonon coupling at the Te 5*p* hole pocket in $TiTe_2$

O. Fedchenko,[1] D. Vasilyev,[1] D. Kutnyakhov,[1] S. Babenkov,[1] S. Chernov,[1] T. Grunske,[2] T. Kauerhof,[2] K. von Volkmann,[2] J. Demsar,[1] K. Rossnagel,[3,4] G. Schönhense,[1] and H. J. Elmers[1]

[1]*Institut für Physik, Johannes Gutenberg-Universität Mainz, Staudingerweg 7, D-55099 Mainz, Germany*

[2]*APE GmbH, D-13053 Berlin, Germany*

[3]*Institut für Experimentelle and Angewandte Physik, Christian-Albrechts-Universität zu Kiel, D-24098 Kiel, Germany*

[4]*Ruprecht Haensel Laboratory, Deutsches Elektronen-Synchrotron DESY, 22607 Hamburg, Germany*

(Received 15 February 2023; revised 31 July 2023; accepted 11 September 2023; published 25 September 2023)

We have determined the quasiparticle dispersion for semimetallic 1*T*-$TiTe_2$ at 20 K using time-of-flight momentum microscopy with tunable soft-x-ray excitation and high-resolution momentum microscopy with 6.4 eV ultraviolet excitation. In particular, we have studied the quasiparticle interactions of the electronic states of the Te 5*p*–hole pockets with high Fermi velocity near the Γ point. Kinks in the otherwise parabolic dispersions suggest the onset of many-body interactions at a binding energy of about 30 meV. We attribute these kinks to electron-phonon coupling. Our study complements previously published results on the Ti 3*d* electron pockets near the *M* and *L* points. The electron-phonon coupling parameters ($\lambda = 0.3$–0.8) are in agreement with previously reported values. An apparently nonzero real part of the self-energy at the Fermi level for one of the two bands may be caused by residual charge-density-wave fluctuations.

DOI: 10.1103/PhysRevB.108.115150

I. INTRODUCTION

Transition-metal dichalcogenides (TMDCs) have been studied extensively in the past because of their interesting physical properties [1–4]. These include the occurrence of charge-density waves (CDWs) [5–7] and superconductivity [6,8], as well as large and nonsaturating magnetotransport [9,10] and topological properties [11,12].

1*T*-$TiTe_2$ constitutes an interesting system for several reasons. Bulk $TiTe_2$ shows reference Fermi-liquid behavior [13–19] without a CDW transition and superconductivity [20–22]. Single-layer $TiTe_2$, by contrast, undergoes a CDW phase transition at 92 K [23,24] or 110 K [7], respectively, as recent photoemission studies have shown. Furthermore, experimental and theoretical results suggest that mechanical strain induces CDWs in $TiTe_2$ at room temperature [25], and chemical strain provokes topological phase transitions [26]. Pressure-induced superconductivity was reported in Ref. [27]. These results imply that electron-phonon coupling might also influence electronic states in bulk $TiTe_2$. Finally, theory predicted the appearance of nontrivial topological surface states caused by hydrostatic pressure and isovalent cation substitution [28,29]. Thus, to better understand the electronic properties, an investigation of the electronic structure of 1*T*-$TiTe_2$ with respect to electron-phonon coupling is needed.

Although the crystal structure of 1*T*-$TiTe_2$ is quasi-two-dimensional (quasi-2D), its electronic states show pronounced dispersion along the perpendicular momentum direction [17,30,31], asking for a complete three-dimensional (3D) measurement of the Fermi surface. In the case of increased correlation effects, the spectral function would broaden and develop deviations from the single-electron picture that reflect the interactions with the underlying many-body system. Indeed, it has been reported that electron-phonon scattering in this material may cause deviations from the expected single-particle dispersion of the Ti 3*d* band [16,18,19,30,32]. Yet, it has been pointed out that weak electron-phonon coupling ($\lambda = 0.22$) cannot lead to superconductivity or CDW instabilities, as commonly found in other quasi-2D TMDCs [33]. Direct experimental evidence of weak electron-phonon coupling from angle-resolved photoemission spectroscopy data has been reported in the case of the Ti 3*d* band near the *M* and *L* points [30]. However, comparable information for the Te 5*p* bands near the Γ point is missing so far.

Here, we have used time-of-flight (TOF) momentum microscopy to map the dependence on the perpendicular momentum k_z of the Fermi surface of 1*T*-$TiTe_2$ from the measured spectral function, using photons in the soft-x-ray regime. Then, using high-resolution momentum microscopy with 6.4 eV excitation, we have determined the complex quasiparticle self-energy for electronic states of the Te 5*p* hole pockets between Γ and *A* at one specific k_z value, deriving quantitative information on the characteristic phonon energies and coupling parameters.

II. EXPERIMENT

Clean 1*T*-$TiTe_2$ samples were grown by chemical vapor transport and prepared by tape-based cleavage in ultrahigh vacuum. Photoemission experiments in the soft-x-ray regime were performed at beamline P04 of the PETRA III storage ring (DESY, Hamburg). Here, we present data taken at photon energies in the range of 216–313 eV at an incidence angle of 22° with respect to the surface plane. The photon momentum vector and the surface normal spanned the *xz*-plane, which coincided with the Γ-*M* azimuth of the crystal surface. For the detection of photoelectrons, we applied TOF momentum microscopy; for details, see Refs. [34,35]. The method al-

lows simultaneous detection of the photoemission intensity $I(E_B, k_x, k_y)$ as a function of momentum components k_x and k_y (parallel to the sample surface), and binding energy E_B.

For high-resolution experiments with photon excitation at 6.4 eV, we applied a combination of a hemispherical analyzer (mean radius of 225 mm) and the TOF detection scheme [36]. The leading aberration term in a hemispherical analyzer, which limits the resolution in the conventional analyzing mode, is the α^2-aberration resulting from electrons entering the analyzer through the entrance slit at an angle α with respect to normal incidence. In the momentum imaging mode, this aberration results in a defined, momentum-dependent energy shift, which we corrected numerically. The flight time dispersion in the hemispherical analyzer also depends on the entrance angle α, and it is also corrected numerically (see Ref. [36] for more details).

The instrument simultaneously captures 3D data arrays $I(E_B, k_x, k_y)$ in an energy interval set by the pass energy and the exit slit of the dispersive spectrometer. For the present experiment, we set an energy interval of 250 meV. The pulsed 6.4-eV laser had a repetition rate of 80 MHz and a corresponding pulse separation of 12.5 ns. The time resolution of the delay-line detector (200 ps) then allowed us to resolve 62 energy points. In the present experiment, we set the drift energy to 10 eV allowing the separation of two consecutive electron bunches, resulting in an energy resolution of 9 meV [36,37]. All photoemission measurements were carried out at a sample temperature of 20 K.

III. RESULTS AND DISCUSSION

Figure 1(b) shows the Fermi surface of 1*T*-$TiTe_2$, recorded at the P04 beamline, at 20 K as a 3D photoemission intensity map. The 3D Fermi surface has been measured by concatenating 3D data arrays recorded at many photon energies between 260 and 313 eV, as described in Ref. [38]. The Fermi surface reveals a threefold symmetry corresponding to the crystal symmetry [Fig. 1(a)]. The columnar sheets centered at the M and M' points exhibit elliptical cross sections with their long axes pointing towards the Γ point. These columnar sheets originate from Ti 3*d* orbitals with d_{z^2} character mixed with d_{xz} and d_{yz} orbitals [39]. The columnar sheet with a rounded cross section centered on the Γ point is derived from Te 5*p* orbitals. For soft-x-ray excitation, the splitting of the columnar sheet is not resolved. Photoemission data with 6.4 eV excitation shown in Fig. 2 resolve two separate sheets, with mainly p_x and p_y character for the inner sheet, and p_z character for the outer sheet in the Γ-*K*-*M* plane, and inverted orbital character for the *A*-*H*-*L* plane [23].

The columnar structures are indicative of the quasi-2D character of these electronic states with a weak dispersion along k_z. Figures 1(c)–1(e) depict cuts through the Fermi surface at different k_z values corresponding to the high-symmetry planes *A*-*H*-*L* and Γ-*K*-*M*, revealing a sixfold symmetry, and to an intermediate plane through $k_z = 0.25G_{001}$, showing the three-fold symmetry of the crystal structure.

Figure 2 presents the high-resolution photoemission data obtained at a photon energy of 6.4 eV. Figure 2(a) shows the 2D Fermi surface map in the k_x-k_y plane. The threefold symmetry indicates that the perpendicular momentum, cor-

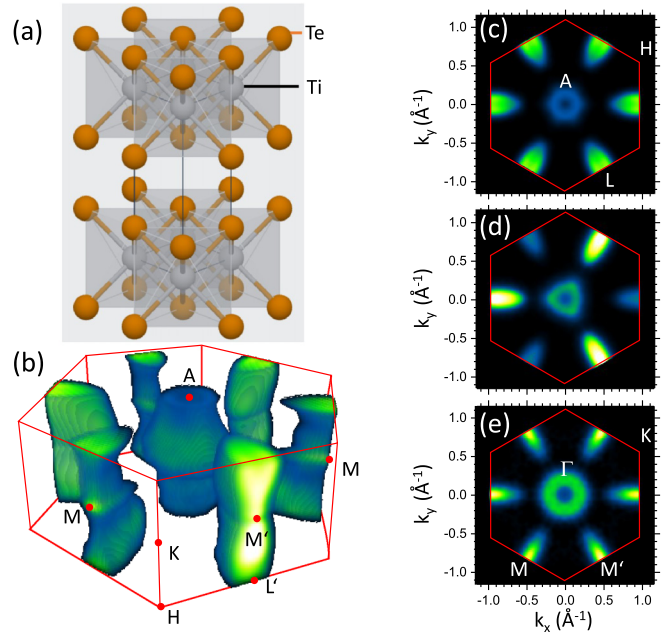

FIG. 1. (a) Schematic crystal structure of 1*T*-$TiTe_2$. (b) Measured Fermi surface and schematic Brillouin zone of 1*T*-$TiTe_2$: Photoemission data from momentum microscopy as a function of photon energy in the range of $h\nu = 260$–313 eV. Data were symmetrized with respect to the crystal structure. [(c)–(e)] Planar cuts through the Fermi surface perpendicular to the Γ-*A* direction at the A-point, $k_z = 0.5G_{001}$ (c), at $k_z = 0.25G_{001}$ (d), and at the Γ-point, $k_z = 0G_{001}$ (e).

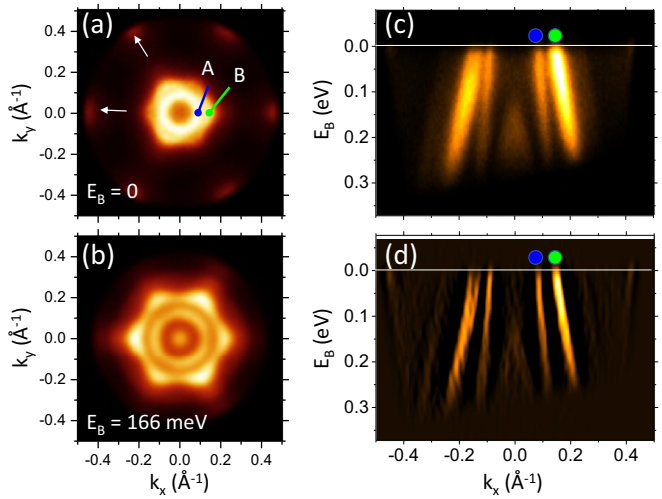

FIG. 2. (a) Constant energy map at a binding energy of $E_B = 0$ of 1*T*-$TiTe_2$ in the k_x-k_y plane (symmetrized according to the crystal symmetry), recorded at a photon energy of 6.4 eV. Labels A and B mark Te 5*p*-hole states. Arrows point to the tips of the Ti 3*d*-electron pockets appearing at the photoemission horizon. (b) Corresponding momentum map at $E_B = 166$ meV. (c) E_B-vs-k_x section along the M'-Γ-M direction. The energy resolution is 9 meV. (d) 2D second derivative of the measured results shown in (c) to enhance areas of weak intensity, while maintaining the band dispersion. Blue and green dots mark the Fermi vectors for band A and band B, respectively.

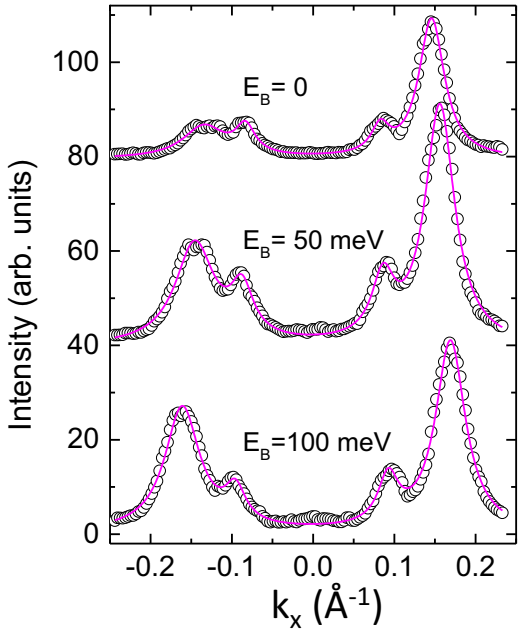

FIG. 3. Momentum distribution curves derived from the data shown in Fig. 2(c) at the indicated binding energies (open circles). Fits to the experimental data with four Lorentzian functions result in the solid pink lines.

responding to the photon energy of 6.4 eV, lies in between the high-symmetry points Γ and A. At this photon energy, the field of view in momentum space is limited by the photoemission horizon being smaller than the Brillouin zone. As a consequence, one observes just the low-intensity tips of the electron pockets centered at the M and L and at the M' and L' points, respectively. At higher binding energy, the central Fermi surface sheets disperse to larger parallel momentum, revealing two separated rings. The outer ring (B) shows protrusions along the Γ-M and Γ-M' directions, while the inner ring (A) is almost circular.

Figure 2(c) depicts the dispersions of band A and band B near the Fermi level, which display an almost linear behavior. To reveal further details, we show the 2D second derivative of the measured photoemission intensity in Fig. 2(d). While the inner band A appears as a single band in opposite k-directions, band B splits near E_F into two separate bands along the Γ-M' direction. These observations are in agreement with previously reported experimental and theoretical data [13–19].

To determine many-body effects acting on the electronic states, we extracted momentum distribution curves (MDCs) along the Γ-M direction at constant binding energies integrated over an interval of 4.5 meV. Raw, nonsymmetrized data (see Fig. 3) are used to avoid any broadening that may be caused by imperfect centering or image aberrations. We then fit the MDCs with four Lorentzian functions for the two bands A and B with positive and negative momentum k_x. Note that the split band B for $k_x < 0$ is fit by a single peak function. MDCs and fits are depicted in Fig. 3 for three selected binding energies. The fits convincingly reproduce the experimental MDCs for positive momentum values. In contrast, the splitting of band B causes broader maxima at negative momentum values and higher binding energies that are not well described by a single Lorentzian function. In the following, we focus on data for positive momentum values, avoiding the discussion of the split peaks.

The fits with the Lorentzian functions result in the parameters k_m and w representing the center position of the MDC peak and its full width at half-maximum at the energy $E_m = E - E_F = -E_B$, respectively. Values for k_m are shown in Figs. 4(a) and 4(b) for both bands A and B. The observed dispersion cannot be described by a parabolic dispersion. Figure 4(d), which shows the photoemission intensity divided by the momentum-integrated intensity of the same data given in Fig. 4(b), reveals a complementary fingerprint of the deviation of the electronic bands from the single-electron behavior. The deviation from the parabolic behavior, indicated by an arrow in Fig. 4(d), is clearly visible for band A. Note that band A also shows a band narrowing near the Fermi level.

The one-electron spectral function $A(k, E)$, measured in our experiment under the assumption of a nearly constant photoemission matrix element, maps the probability that the initial N-electron state, from which one electron has been instantly removed, is a ground state of the final $(N-1)$-particle system. The interactions in the underlying many-body system are conveniently described by the complex quasiparticle self-energy $\Sigma(E) = \mathrm{Re}[\Sigma(E)] + i\,\mathrm{Im}[\Sigma(E)]$. The real part describes the renormalization of the electron dispersion and the imaginary part the lifetime of the hole created by the excitation. Assuming that $\Sigma(E)$ depends only on the energy, the spectral function is given by

$$A(k,E) = -\frac{1}{\pi}\frac{\mathrm{Re}\Sigma(E)}{[E - E_0(k) - \mathrm{Re}\Sigma(E)]^2 + [\mathrm{Im}\Sigma(E)]^2}. \quad (1)$$

The scan along the chosen direction in momentum space directly measures $A(k_x, E)$. The real and imaginary parts of $\Sigma(E_m)$ at a constant energy E_m are then determined from the set of equations

$$\mathrm{Re}\Sigma(E_m) = E_m - E_0(k_m), \quad (2)$$

$$\mathrm{Im}\Sigma(E_m) = 1/2[E_0(k_m + w/2)] - [E_0(k_m - w/2)]. \quad (3)$$

We assume that the bare band dispersion over a narrow range near E_F is described by a quadratic polynomial function, where we find the Fermi velocity, v_F, and the Fermi wave vector, k_F, from a parabolic fit to the dispersion at binding energies $E_B > 50$ meV.

The corresponding results of the complex quasiparticle self-energy are depicted in Figs. 4(e) and 4(f). For both bands A and B, the real part of $\Sigma(E)$ deviates from zero for binding energies below about 50 meV, setting the energy scale for the many-body interactions. We find that band A exhibits larger maximum values of $\Sigma(E)$ as compared to band B.

For quasi-2D electron states, as we assumed here, the contribution to the linewidth due to final-state broadening may be neglected because of the weak k_z dispersion [40]. However, the free-electron final state model has been questioned by electron diffraction experiments [41]. The final states of $TiTe_2$ indeed show strong non-free-electron effects due to scattering off its highly modulated quasi-2D crystal potential. The final states feature a multiband structure, each of the bands showing significantly nonparabolic dispersion. Indeed, these findings can modify the conclusions drawn

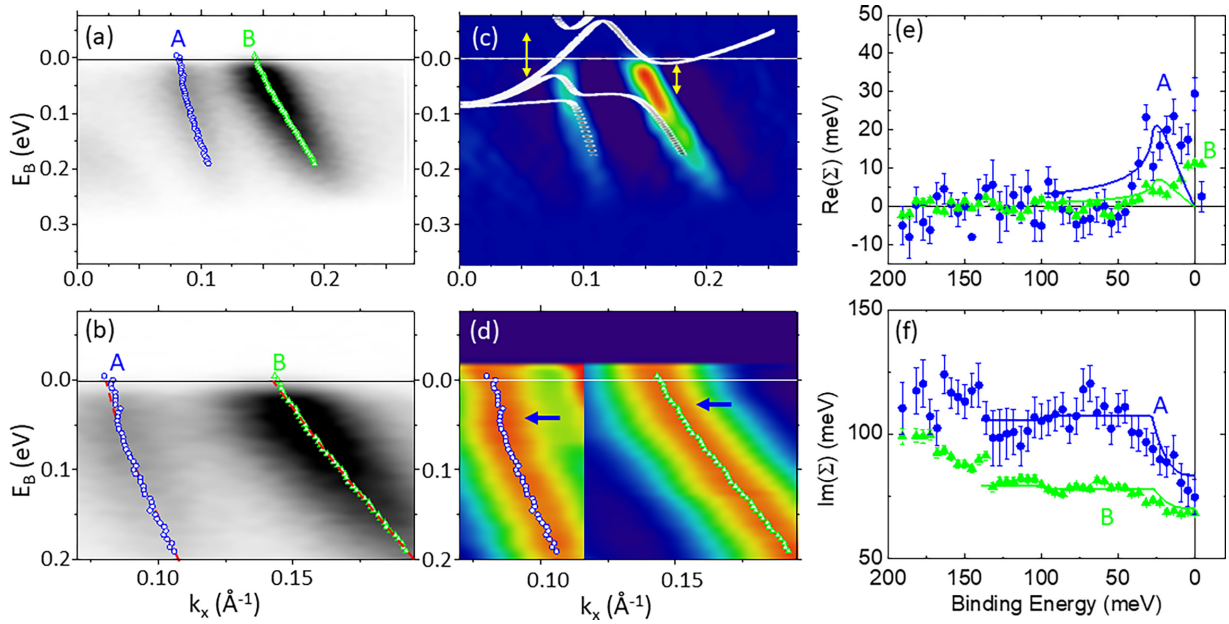

FIG. 4. (a) E_B-vs-k_x section of the photoemission intensity array along the Γ-M direction. Open blue circles and green triangles represent the peak centers resulting from the numerical fits similar to the ones shown in Fig. 3 for the two bands A and B. (b) Detailed view of (a). The red dashed lines indicate the parabolic dispersion derived from a fit to a quadratic polynomial function of data points for $E_B > 0.05$ eV for both bands. (c) Second derivative of the photoemission intensity shown in (a), represented in a color code (blue, low intensity; red, high intensity). Band overlay (white and gray dots) corresponds to the calculated hybridization of Te 5p states with backfolded Ti 3d states, adapted from Ref. [23]. (d) Photoemission intensity divided by the momentum-integrated photoemission intensity [color code as in (c) and adapted for the different intensity for bands A and B]. Blue arrows indicate the onset of the deviation from the parabolic dispersion. (e),(f) Real and imaginary part of the quasiparticle self-energy $\Sigma(-E_B)$ derived from the experimental dispersion assuming a parabolic dispersion for the bare band. Full blue (A) and green (B) lines in (f) indicate simultaneous fits of Re$[\Sigma(-E_B)]$ and Im$[\Sigma(-E_B)]$ using the Debye model.

from assuming free-electron-like final states. In the case of $TiTe_2$, the final states have been determined experimentally [41]. There is only a single final state in the energy range accessible by the photon energy. Therefore, a broadening due to multiple final states can be excluded. The k_z value determined from the free-electron final state, assuming an inner potential of 10 eV with respect to the Fermi level, agrees with the k_z value determined from the results reported in Ref. [41].

The lifetime broadening upon approaching E_F derived from electron-phonon and electron-electron interactions vanishes at low temperature [42–44]. Therefore, the lifetime broadening observed at E_F predominantly originates from electron-defect interaction. We obtain $\mathrm{Im}[\Sigma_{\mathrm{ed}}(E_F)] = \Gamma_{\mathrm{ed}} = 75$ meV for band A and 60 meV for band B. Γ_{ed} is assumed to be independent of E_B and k. The remaining energy-dependent part of $\mathrm{Im}[\Sigma_{\mathrm{ed}}(E)]$ is attributed to electron-phonon interaction.

The slope of the bare band dispersion at E_F was evaluated as $dE/dk = \hbar v_F = 6.5$ eV Å for band A and 3.4 eV Å for band B. The lifetimes of the electronic states at E_F are $\tau = \hbar/\Gamma_{\mathrm{ed}} = 0.8 \times 10^{-14}$ s (band A) and 1.1×10^{-14} s (band B) at 20 K. The mobility of the electrons in these states can be evaluated as $\mu = e\tau/m^* \approx 100$ cm^2/V s (band A) and 300 cm^2/V s (band B) with $m^*/m = 0.12$ (0.05). The extracted mobility is very small compared to values of 10^7 cm^2/V s determined for a high-mobility 2D electron gas at a semiconductor interface [45]. On the other hand, the mobility is comparable to that of a Cu surface state [46].

These values are unrealistically high in view of previously reported much smaller coupling parameters $\lambda_{\mathrm{ep}} < 0.5$ [20–22].

We then fit $\mathrm{Im}[\Sigma_{\mathrm{ed}}(E)]$ and $\mathrm{Re}[\Sigma_{\mathrm{ed}}(E)]$ with the self-energy according to a Debye-model with a set of three parameters: the electron-phonon coupling parameter λ_{ep}, Debye-energy ω_D, and an offset Γ_{ed} for the electron-defect interaction [19]. The fit results in the values $\lambda_{A,\mathrm{ep}} = 0.8(2)$, $\omega_{A,D} = 28(2)$ meV, and $\Gamma_{A,\mathrm{ed}} = 81(3)$ meV for band A. Numbers in parentheses correspond to standard deviations resulting from the fit. For band B, we obtain $\lambda_{B,\mathrm{ep}} = 0.3(1)$, $\omega_{B,D} = 27(2)$ meV, and $\Gamma_{B,\mathrm{ed}} = 68(1)$ meV, respectively. The resulting fits describe the experimental data sufficiently well [see Fig. 4(f)] in the case of band A. The deviation of $\mathrm{Re}[\Sigma_{\mathrm{ed}}(E)]$ from the Debye model in the case of band B is discussed below. We note that the fit parameters for the electron-phonon coupling are realistic and in agreement with previously reported values [20–22].

Experimentally reported phonon energies using Raman spectroscopy are up to 18 meV [47] and thus smaller than the values determined here by the fit to the Debye model. However, electron-phonon coupling includes the odd phonon modes that are not Raman-active. Odd phonon energies instead are up to 32 meV [48]. Considering even and odd phonon modes, our experimentally obtained values of 28 meV (band A) and 27 meV (band B) agree with previously reported values for phonon energies in 1T-$TiTe_2$.

The reason for $\mathrm{Re}[\Sigma_{ed}(E)]$ not to approach zero at E_F in the case of band B remains unclear. We speculate that a Te

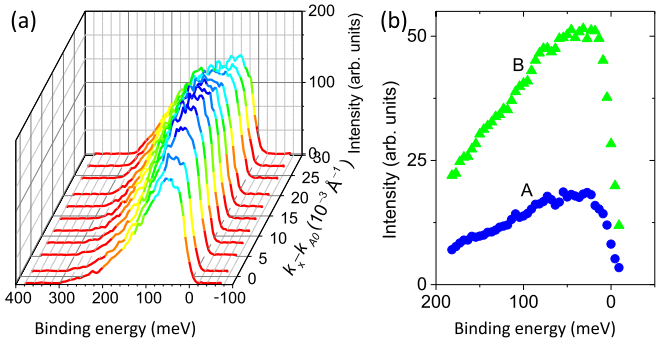

FIG. 5. (a) Energy distribution curves near band A extracted from the data shown in Fig. 4, where $k_x - k_{A0}$ denotes the difference of the parallel momentum k_x and the bare band Fermi vector k_{A0}. (b) Peak areas of bands A and B as derived from the peak fitting of momentum distribution curves vs binding energy.

5p–Ti 3d band hybridization perturbs the band dispersions for band B, similar to what has been observed in the $TiTe_2$ monolayer [23]. In the monolayer case, the band hybridization is a result of backfolded Ti 3d bands due to the formation of a (2×2) CDW. Although the CDW transition is suppressed in bulk $TiTe_2$, weak CDW fluctuations could still be present at 20 K. The decrease of the photoemission intensity in the same energy range close to E_F, in contrast to the expected intensity increase as a result of the formation of a well-defined quasiparticle state, may support this explanation as discussed in the following.

The onset of hybridization with backfolded Ti 3d bands due to a fluctuating CDW, as observed for a $TiTe_2$ monolayer [23], would open energy gaps for bands A and B near the Fermi level [see Fig. 4(c)]. These gaps suppress the photoemission intensity in the gap regions. The energy gaps roughly coincide with the quasiparticle states expected for electron-phonon coupling.

The suppression of the quasiparticle states is reinforced by plotting the energy distribution curves [Fig. 5(a)] close to the Fermi vector of band A. Furthermore, the fitted peak areas for peak A in the momentum distribution curves, shown in Fig. 5(b), reveal a decrease in photoemission intensity close E_F, in agreement with the hybridization model. The hybridization model can thus in principle explain why the photoemission intensity from the quasiparticle peak is absent in the energy region close to the Fermi level.

IV. SUMMARY

In summary, TOF momentum microscopy in the soft-x-ray regime reveals pronounced deviations from a 2D character of electronic states in 1T-$TiTe_2$. Constant energy maps exhibit a sixfold symmetry for cuts through the high-symmetry points Γ and A, whereas constant-energy cuts at intermediate k_z values reveal a threefold symmetry, consistent with the crystal symmetry. We have analyzed high-resolution data obtained with 6.4 eV photon energy excitation using a complex self-energy ansatz for Te 5p hole bands between the Γ and the A point. We identified electron-phonon interaction as the predominant many-body interaction responsible for the energy dependence of the self-energy. Fitting the real and imaginary parts of the self-energy to the Debye model results in characteristic phonon energies of 28 meV and electron-phonon coupling parameters $\lambda = 0.8$ (band A) and $\lambda = 0.3$ (band B), respectively. Residual CDW fluctuations at low temperature may be responsible for an apparent finite value of the real part of the self-energy at the Fermi level in the case of the outer hole band. The experimental data thus reveal electron-phonon coupling parameters that suggest that many-body effects play an important role for electronic properties in bulk $TiTe_2$.

ACKNOWLEDGMENTS

This work was funded by the Deutsche Forschungsgemeinschaft (DFG, German Research Foundation) Grant No. TRR288422213477 (Projects No. B04, No. B08), and by the BMBF (Projects No. 05K22UM4 and No. 05K19UM2). O.F. acknowledges funding from TopDyn.

[1] B. Sipos, A.F. Kusmartseva, A. Akrap, H. Berger, L. Forro, and E. Tutis, From Mott state to superconductivity in 1T-TaS_2, Nat. Mater. **7**, 960 (2008).

[2] K. F. Mak, K. He, J. Shan, and T. F. Heinz, Control of valley polarization in monolayer MoS_2 by optical helicity, Nat. Nanotechnol. **7**, 494 (2012).

[3] M. N. Ali, J. Xiong, S. Flynn, J. Tao, Q. D. Gibson, L. M. Schoop, T. Liang, N. Haldolaarachchige, M. Hirschberger, N. P. Ong, and R. J. Cava, Large, non-saturating magnetoresistance in WTe_2, Nature (London) **514**, 205 (2014).

[4] M. Bonilla, S. Kolekar, Y. Ma, H. C. Diaz, V. Kalappattil, R. Das, T. Eggers, H. R. Gutierrez, M. Phan, and M. Batzill, Strong room-temperature ferromagnetism in VSe_2 monolayers on van der Waals substrates, Nat. Nanotechnol. **13**, 289 (2018).

[5] S. Bocharov, G. Dräger, D. Heumann, A. Šimůnek, and O. Šipr, Polarized x-ray-absorption spectra of TiS_2, $TiSe_2$, and $TiTe_2$, Phys. Rev. B **58**, 7668 (1998).

[6] C. S. Cucinotta, K. Dolui, H. Pettersson, Q. M. Ramasse, E. Long, S. E. O'Brian, V. Nicolosi, and S. Sanvito, Electronic properties and chemical reactivity of TiS_2 nanoflakes, J. Phys. Chem. C **119**, 15707 (2015).

[7] B. Singh, C.-H. Hsu, W.-F. Tsai, V. M. Pereira, and H. Lin, Stable charge density wave phase in a 1T-$TiSe_2$ monolayer, Phys. Rev. B **95**, 245136 (2017).

[8] K. H. Park, J. Choi, H. J. Kim, D.-H. Oh, J. R. Ahn, and S. U. Son, Unstable single-layered colloidal TiS_2 nanodisks, Small **4**, 945 (2008).

[9] J. Sun, R. S. Deacon, W. Luo, Y. Yuan, X. Liu, H. Xie, Y. Gao, and K. Ishibashi, Asymmetric fermi velocity induced chiral magnetotransport anisotropy in the type-II dirac semi-metal $PtSe_2$, Commun. Phys. **3**, 93 (2020).

[10] J. Zhong, J. Yu, L. Cao, C. Zeng, J. Ding, C. Cong, Z. Liu, and Y. Liu, High-performance polarization-sensitive photodetector

based on a few-layered $PdSe_2$ nanosheet, Nano Res. **13**, 1780 (2020).

[11] B. Radisavljevic, A. Radenovic, J. Brivio, V. Giacometti, and A. Kis, Single-layer MoS_2 transistors, Nat. Nanotechnol. **6**, 147 (2011).

[12] Q. H. Wang, K. Kalantar-Zadeh, A. Kis, J. N. Coleman, and M. S. Strano, Electronics and optoelectronics of two-dimensional transition metal dichalcogenides, Nat. Nanotechnol. **7**, 699 (2012).

[13] R. Claessen, R. O. Anderson, J. W. Allen, C. G. Olson, C. Janowitz, W. P. Ellis, S. Harm, M. Kalning, R Manzke, and M. Skibowski, Fermi-Liquid Line Shapes Measured by Angle-Resolved Photoemission Spectroscopy on $1T$-$TiTe_2$, Phys. Rev. Lett. **69**, 808 (1992).

[14] J. W. Allen, G. H. Gweon, R. Claessen, and K. Matho, Fermi liquids and non-fermi liquids: The view from photoemission, J. Phys. Chem. Solids **56**, 1849 (1995).

[15] R. Claessen, R. O. Anderson, G.-H. Gweon, J. W. Allen, W. P. Ellis, C. Janowitz, C. G. Olson, Z. X. Shen, V. Eyert, M. Skibowski, K. Friemelt, E. Bucher, and S. Hüfner, Complete band-structure determination of the quasi-two-dimensional fermi-liquid reference compound $TiTe_2$, Phys. Rev. B **54**, 2453 (1996).

[16] L. Perfetti, C. Rojas, A. Reginelli, L. Gavioli, H. Berger, G. Margaritondo, M. Grioni, R. Gaál, L. Forró, and F. Rullier Albenque, High-resolution angle-resolved photoemission investigation of the quasiparticle scattering processes in a model fermi liquid: $1T$-$TiTe_2$, Phys. Rev. B **64**, 115102 (2001).

[17] K. Rossnagel, L. Kipp, M. Skibowski, C. Solterbeck, T. Strasser, W. Schattke, D. Voß, P. Krüger, A. Mazur, and J. Pollmann, Three-dimensional fermi surface determination by angle-resolved photoelectron spectroscopy, Phys. Rev. B **63**, 125104 (2001).

[18] L. Perfetti, C. Rojas, A. Refinelli, L. Gavioli, H. Berger, G. Margaritondo, and M. Grioni, Quasiparticle Scattering Processes in a Model Fermi Liquid: $1T$-$TiTe_2$, Surf. Rev. Lett. **09**, 1117 (2002).

[19] G. Nicolay, B. Eltner, S. Hüfner, F. Reinert, U. Probst, and E. Bucher, Importance of many-body effects to the spectral function of $1T$-$TiTe_2$, Phys. Rev. B **73**, 045116 (2006).

[20] H. Wang, L. Yu, Y.-H. Lee, Y. Shi, A. Hsu, M. L. Chin, L.-J. Li, M. Dubey, J. Kong, and T. Palacios, Integrated circuits based on bilayer MoS_2 transistors, Nano Lett. **12**, 4674 (2012).

[21] A. K. Geim and I. V. Grigorieva, Van der waals heterostructures, Nature (London) **499**, 419 (2013).

[22] P. Goli, J. Khan, D. Wickramaratne, R. K. Lake, and A. A. Balandin, Charge density waves in exfoliated films of van der waals materials: Evolution of raman spectrum in $TiSe_2$, Nano Lett. **12**, 5941 (2012).

[23] T. Antonelli, W. Rahim, M. D. Watson, A. Rajan, O. J. Clark, A. Danilenko, K. Underwood, I. Marković, E. Abarca-Morales, S. R. Kavanagh, P. Le Fèvre, F. Bertran, K. Rossnagel, D. O. Scanlon, and P. D. C. King, Orbital-selective band hybridisation at the charge density wave transition in monolayer $TiTe_2$, npj Quantum Mater. **7**, 98 (2022).

[24] P. Chen, W. W. Pai, Y.-H. Chan, A. Takayama, C.-Z. Xu, A. Karn, S. Hasegawa, M. Y. Chou, S.-K. Mo, A.-V. Fedorov, and T.-C. Chiang, Emergence of charge density waves and a pseudogap in single-layer $TiTe_2$, Nat. Commun. **8**, 516 (2017).

[25] S. Fragkos, R. Sant, C. Alvarez, A. Bosak, P. Tsipas, D. Tsoutsou, H. Okuno, G. Renaud, and A. Dimoulas, Room temperature commensurate charge density wave in epitaxial strained $TiTe_2$ multilayer films, Adv. Mater. Interfaces **6**, 1801850 (2019).

[26] Z. Zhu, Y. Cheng, and U. Schwingenschlogl, Topological Phase Diagrams of Bulk and Monolayer $TiS_{2-x}Te_x$, Phys. Rev. Lett. **110**, 077202 (2013).

[27] U. Dutta, P. S. Malavi, S. Sahoo, B. Joseph, and S. Karmakar, Pressure-induced superconductivity in semimetallic $1T$-$TiTe_2$, Phys. Rev. B **97**, 060503(R) (2018).

[28] Q. Zhang, Y. Cheng, and U. Schwingenschlogl, Series of topological phase transitions in $TiTe_2$ under strain, Phys. Rev. B **88**, 155317 (2013).

[29] M. Zhang, X. Wang, A. Rahman, Q. Zeng, D. Huang, R. Dai, Z. Wang, and Z. Zhang, Pressure-induced topological phase transitions and structural transition in $1T$-$TiTe_2$ single crystal, Appl. Phys. Lett. **112**, 041907 (2018).

[30] X.-F. Tang, Y.-X. Duan, F.-Y. Wu, S.-Y. Liu, C. Zhang, Y.-Z. Zhao, J.-J. Song, Y. Luo, Q.-Y. Wu, J. He, H. Y. Liu, W. Xu, and J.-Q. Meng, Three-dimensional fermi surface and electron-phonon coupling in semimetallic $1T$-$TiTe_2$ studied by angle-resolved photoemission spectroscopy, Phys. Rev. B **99**, 125112 (2019).

[31] S. Borisenko, A. Fedorov, A. Kuibarov, M. Bianchi, V. Bezguba, P. Majchrzak, P. Hofmann, P. Baumgartel, V. Voroshnin, Y. Kushnirenko, J. Sánchez-Barriga, A. Varykhalov, R. Ovsyannikov, I. Morozov, S. Aswartham, O. Feia, L. Harnagea, S. Wurmehl, A. Kordyuk, A. Yaresko *et al.*, Fermi surface tomography, Nat. Commun. **13**, 4132 (2022).

[32] S.-X. Zhu, C. Zhang, Q.-Y. Wu, X.-F. Tang, H. Liu, Z.-T. Liu, Y. Luo, J.-J. Song, F.-Y. Wu, Y.-Z. Zhao, S.-Y. Liu, T. Le, X. Lu, H. Ma, K.-H. Liu, Y.-H. Yuan, H. Huang, J. He, H. Y. Liu, Y.-X. Duan *et al.*, Temperature evolution of quasiparticle dispersion and dynamics in semimetallic $1T$-$TiTe_2$ via high-resolution angle-resolved photoemission spectroscopy and ultrafast optical pump-probe spectroscopy, Phys. Rev. B **103**, 115108 (2021).

[33] K Rossnagel, On the origin of charge-density waves in select layered transition-metal dichalcogenides, J. Phys.: Condens. Matter **23**, 213001 (2011).

[34] G. Schönhense, K. Medjanik, S. Chernov, D. Kutnyakhov, O. Fedchenko, M. Ellguth, D. Vasilyev, A. Zaporozhchenko-Zymaková, D. Panzer, A. Oelsner, C. Tusche, B. Schonhense, J. Braun, J. Minár, H. Ebert, J. Viefhaus, W. Wurth, and H. J. Elmers, Spin-filtered time-of-flight k-space microscopy of Ir - Towards the complete photoemission experiment, Ultramicroscopy **183**, 19 (2017).

[35] G. Schonhense, K. Medjanik, and H.-J. Elmers, Space-, time- and spin-resolved photoemission, J. Electron Spectrosc. Relat. Phenom. **200**, 94 (2015).

[36] G. Schönhense, S. Babenkov, D. Vasilyev, H.-J. Elmers, and K. Medjanik, Single-hemisphere photoelectron momentum microscope with time-of-flight recording, Rev. Sci. Instrum. **91**, 123110 (2020).

[37] G. Schönhense, K. Medjanik, O. Fedchenko, A. Zymaková, S. Chernov, D. Kutnyakhov, D. Vasilyev, S. Babenkov, H. J. Elmers, P. Baumgartel, P. Goslawski, G. Ohrwall, T. Grunske, T. Kauerhof, K. von Volkmann, M. Kallmayer, M. Ellguth, and A. Oelsner, Time-of-flight photoelectron momentum microscopy

with 80-500 MHz photon sources: Electron-optical pulse picker or bandpass pre-filter, J. Synch. Radiat. **28**, 1891 (2021).

[38] K. Medjanik, O. Fedchenko, S. Chernov, D. Kutnyakhov, M. Ellguth, A. Oelsner, B. Schonhense, T. R. F. Peixoto, P. Lutz, C.-H. Min, F. Reinert, S. Daester, Y. Acremann, J. Viefhaus, W. Wurth, H. J. Elmers, and G. Schonhense, Direct 3d mapping of the fermi surface and fermi-velocity, Nat. Mater. **16**, 615 (2017).

[39] S. Beaulieu, M. Schüler, J. Schusser, S. Dong, T. Pincelli, J. Maklar, A. Neef, F. Reinert, M. Wolf, L. Rettig, J. Minár, and R. Ernstorfer, Unveiling the orbital texture of 1T-$TiTe_2$ using intrinsic linear dichroism in multidimensional photoemission spectroscopy, npj Quantum Mater. **6**, 93 (2021).

[40] N. V. Smith, P. Thiry, and Y. Petroff, Photoemission linewidths and quasiparticle lifetimes, Phys. Rev. B **47**, 15476 (1993).

[41] V. N. Strocov, E. E. Krasovskii, W. Schattke, N. Barrett, H. Berger, D. Schrupp, and R. Claessen, Three-dimensional band structure of layered $TiTe_2$: Photoemission final-state effects, Phys. Rev. B **74**, 195125 (2006).

[42] A. Eiguren, B. Hellsing, F. Reinert, G. Nicolay, E. V. Chulkov, V. M. Silkin, S. Hüfner, and P. M. Echenique, Role of Bulk and Surface Phonons in the Decay of Metal Surface States, Phys. Rev. Lett. **88**, 066805 (2002).

[43] A. Eiguren, B. Hellsing, E. V. Chulkov, and P. M. Echenique, Phonon-mediated decay of metal surface states, Phys. Rev. B **67**, 235423 (2003).

[44] E. E. Krasovskii, K. Rossnagel, A. Fedorov, W. Schattke, and L. Kipp, Determination of The Hole Lifetime from Photoemission: Ti 3d States in $Tite_2$, Phys. Rev. Lett. **98**, 217604 (2007).

[45] W. Pan, N. Masuhara, N. S. Sullivan, K. W. Baldwin, K. W. West, L. N. Pfeiffer, and D. C. Tsui, Impact of Disorder on the 5/2 Fractional Quantum Hall State, Phys. Rev. Lett. **106**, 206806 (2011).

[46] J. Jiang, S. S. Tsirkin, K. Shimada, H. Iwasawa, M. Arita, H. Anzai, H. Namatame, M. Taniguchi, I. Yu. Sklyadneva, R. Heid, K.-P. Bohnen, P. M. Echenique, and E. V. Chulkov, Many-body interactions and rashba splitting of the surface state on Cu(110), Phys. Rev. B **89**, 085404 (2014).

[47] M. Hangyo, S.-I. Nakashima, and A. Mitsuishi, Raman spectroscopic studies of MX2-type layered compounds, Ferroelectrics **52**, 151 (1983).

[48] H. Ding and B. Xu, Structural, elastic, and vibrational properties of layered titanium dichalcogenides: A van der waals density functional study, J. Chem. Phys. **137**, 224509 (2012).